SEMARAK ILMU PUBLISHING

CFD Letters

Journal homepage:
https://semarakilmu.com.my/journals/index.php/CFD_Letters/index
ISSN: 2180-1363

Numerical Investigation of Flow Around Finite Height Rectangular

La Ode Ahmad Barata[1,*], Takahiro Kiwata[2], Aditya Rachman[3], Samhuddin[1], Nanang Endriatno[1]

[1] Department of Mechanical Engineering, Halu Oleo University, Kendari 93232, Indonesia
[2] Institute of Science and Engineering, Kanazawa University, Japan
[3] Mechanical Engineering, Wollongong University, Australia

ARTICLE INFO

Article history:
Received 26 September 2022
Received in revised form 23 October 2022
Accepted 18 November 2022
Available online 1 June 2023

Keywords:
Slender rectangular; Numerical Investigation; LES; flow-field; flow features

ABSTRACT

Three-dimensional flow features of the slender rectangular prism with cross-section height (*H*) to streamwise depth (*D*) ratio or side ratio (*D/H* = 0.5) were investigated numerically using the Large-eddy simulations (*LES*) turbulence model with Reynolds number Re = 22000. Four different aspect ratios (*L/H* = 2.5 – 10) were employed in this research to study the effect of the spanwise variation of the prism model on the flow pattern around the prism. Moreover, the instability-induced motion of the prism was modeled to predict the alteration of flow characteristics of stationary to vibrating states of the test model. The global quantities such as drag force, pressure coefficient, and Strouhal frequency characteristics are presented, which suggests that the structure end tip effect plays an essential role in the dependency of flow features variation. The velocity vector variations at streamwise and spanwise positions are also demonstrated. The prism model with a small aspect ratio (*L/H* = 2.5) exhibited Karman vortex suppression at the prism's vicinity, and the streamwise vortices region shrank. The flow features of the vibrating prism show different behaviors from the stationary prism model.

1. Introduction

Flow behavior around the blunt prism is considerably paid attention because of its effect on many engineering structures, such as rigid or dynamic structures, heat exchangers, masts, long piping systems, marine risers, chimneys, cooling towers, and tall buildings. The behavior of the flow structure around the cylindrical or prismatic shapes can be found in literature, both numeric and experimental studies, such as references [1-3]. Structure failure due to the flow-induced vibration is closed related to the structure response on the incoming flow stream. For instance, the failure of the Tacoma narrow bridge [4]. Flow stream around the cylinder can also create aeolian tone noise, which makes environmental noise issues. Dynamic response behaviors over the structure have been mitigated using the turbulent control parts such as using multiple cylinders in tandem or staggered, stepped, attached endplate, splitter plate, etc. Zdravkovich [5] presented the various ways to suppress vortex shedding over the circular cylinder.

* *Corresponding author.*
E-mail address: ahmad.barata@uho.ac.id (La Ode Ahmad Barata)

https://doi.org/10.37934/cfdl.15.6.154175

Moreover, using multiple cylinders to control the circular cylinder's dynamic response can be found in the researches by Griiffith *et al.,* [6], Ding *et al.,* [7], and Kim and Alam [8]. The prismatic structure equipped with a turbulent control has demonstrated the alteration of flow pattern and dynamic response of elastically mounted structure [9-11]. Flow behavior around the prismatic body has different characteristics from the circular body, which depends on the body shape, length, presence of end tip, and Reynolds number [12-14]. In the case of a rectangular prismatic body with a sharp edge, flow separation occurs at the leading edge, and flow behaviors at the side and behind the prism are considerably influenced by the prism's depth (side ratio). It differs from a circular cylinder because the separation point varies with the Reynolds number [15].

The effect of the cylinder's depth on the flow field characteristics demonstrated that the alteration of flow features such as drag force, pressure coefficient, and Strouhal number is influenced by the prism's depth and Reynolds number. Prism's critical depth to height ratio is around 0.6, as presented in researches by Nakaguchi [15], Okajima *et al.,* [16], and Nakamura and Hirata [17]. Moreover, recent investigations on a depth ratio effect are found in researches by Bruno *et al.,* [18], Tian *et al.,* [19], Liu *et al.,* [20], and Wang *et al.,* [21]. In nature, separated shear layers at the prism's leading edge roll up and reattach on the surface. The symmetric or asymmetric vortices shed behind as the regular Karman vortex. Consequently, Reynolds number, depth to a height ratio or a side ratio, and vortex interaction of flow wake structure are essential to the flow behaviors around prismatic structures.

The rectangular prismatic body is a common shape for a second structure member widely used in construction systems. The presence of an end tip structure alters flow characteristics in the wake, which is different from a two-dimensional one. The end tip condition is also commonly found in civil and architectural construction buildings, airplane winglets, etc.

Studies on the flow characteristics around the prismatic body with an end tip are widely shown by various investigation approaches, such as grounded at a base, pivoted, or mounted at a ceiling tunnel [22-25]. Flow characteristics analysis has shown that the end tip vortex alters the spanwise vortex in the wake. Meanwhile, the alteration of the spanwise vortex is closed related to the prism's length. The critical length is defined as the ratio of span length to cross-section height *L/H* is 5.0. The flow investigations around prismatic structure with free end focus on the square prism. Studies on the free-end effect of the slender rectangular are still entirely unexplored. He *et al.,* [26] presented a numerical approach to the end effect of a circular cylinder with a low aspect ratio. They showed that the presence of an end tip affects fluid force characteristics and the stability response of the cylinder's motion. The span length variation changes the local velocity, wake zone, and vortex periodicity around the prism with a small aspect ratio, mainly at the prism with an aspect ratio smaller than the critical aspect ratio [14].

Meanwhile, there is insufficient analysis of the unsteady flow behavior prediction of flow around slender rectangular prism by the numerical method in the past. Detailed analysis of the flow features around 3D slender rectangular is a challenge to provide partial parts to the comprehensive analysis of the end tip effect. Tian *et al.,* [19] showed that the two-dimensional numerical approach using the unsteady RANS model has been unsuccessful in predicting aerodynamic components around a slender rectangular prism.

Three-dimensional Large Eddy Simulation (*LES*) turbulence model is a robust tool to analyze and visualize the flow-structure interaction of a blunt body from the perspective of academic research [27]. In this study, we investigated the effect of spanwise variation (aspect ratios, *AR*) of a slender rectangular prism on the flow characteristics numerically. Moreover, the instability-induced motion of the rectangular prism was also predicted.

2. Computational Method

The finite volume-based *CFD* code (ANSYS Fluent v18) with an academic license was employed to model the flow behaviors past the rectangular prism. Three-dimensional analysis of turbulent flow characteristics around the free-end rectangular prism was solved using the large eddy simulation turbulence model. The governing equations of incompressible Newtonian flow problems with constant physical properties, i.e., mass and momentum conservations, were solved by the equations below (see also the common governing equations of mass and momentum conservation by Tey *et al.,* [29]).

$$\frac{\partial \overline{u}_i}{\partial x_i} = 0, \tag{1}$$

and spatial filtering Navier-Stokes equation as

$$\frac{\partial u_i}{\partial t} + \frac{\partial}{\partial x_j}\left(\overline{u_i u_j}\right) = -\frac{1}{\rho}\frac{\partial \overline{p}}{\partial x_i} + v\nabla^2 \overline{u}_i, \text{ where } \bar{u} \text{ is solenoidal.} \tag{2}$$

Eq. (2) is adjusted in the common form by considering residual or subgrid-scale stress tensor (τ_{ij}^R) due to the filtering effect.

$$\frac{\partial u_i}{\partial t} + \frac{\partial}{\partial x_j}\left(\overline{u_i u_j}\right) = -\frac{1}{\rho}\frac{\partial \overline{p}}{\partial x_i} + \frac{1}{\rho}\frac{\partial \tau_{ij}^R}{\partial x_j} + v\nabla^2 \overline{u}_i, \tag{3}$$

$$\tau_{ij}^R = \rho\left[\overline{u}_i\overline{u}_j - \overline{u_i u_j}\right] \tag{4}$$

where $\bar{u}$, $\bar{p}$, and v are filtered average velocity vector, pressure, and fluid kinematic viscosity, respectively.

The effect of turbulent motion is lumped into a turbulent viscosity where kinetic energy dissipation at the sub-grid scale (SGS) is considered a molecular diffusion. Nicoud and Ducros [28] introduced near-wall treatment of eddies motion to adapt local eddy viscosity by introducing the *Wall-Adapting Local Eddy-Viscosity* (WALE) model. This model maintains the asymptotic (y^3) near-wall scaling behavior for the turbulent viscosity. Consequently, it yields zero eddy viscosity in wall-bounded flows and is considered to reproduce the transition flow regime. Moreover, it is solely a product of the characteristic length and velocity scale, as shown in Eq. (5) to Eq. (8) [30].

$$v_t = L_s^2 \frac{\left(S_{ij}^d S_{ij}^d\right)^{\frac{3}{2}}}{\left(\overline{S_{ij}^d S_{ij}^d}\right)^{\frac{5}{2}} + \left(S_{ij}^d S_{ij}^d\right)^{\frac{5}{4}}} \tag{5}$$

$$\overline{S_{ij}} = \tfrac{1}{2}\left(\overline{g_{ij}} + \overline{g_{ji}}\right), \tag{6}$$

$$S_{ij}^d = \tfrac{1}{2}\left(\overline{g_{ij}}^2 + \overline{g_{ji}}^2\right) - \tfrac{1}{3}\delta_{ij}\overline{g_{kk}}^2 \tag{7}$$

$$\overline{g_{ij}} = \frac{\partial \bar{u}_i}{\partial x_j}, \tag{8}$$

where the strain tensor and velocity gradient tensor rate ($\bar{s}_{ij}, \bar{g}_{ij,}$) are represented as $L_s = \min(\kappa d, C_w V^{1/3})$, C_w = 0.235, κ = 0.4187 where L_s,κ,d, C_w, V, δ_{ij}, are the length scale, the Karman's constant energy, minimum wall spacing, WALE constant, cell volume, and Kronecker delta ($\delta_{ij} = 0$ if $i \neq j$, otherwise 1 if $i = j$), respectively [30]. This WALE method is adopted in the present study.

Furthermore, the governing equations were discretized based on the finite volume method approach, with the convection term as the bounded center difference. The second-order precision implicit method and the pressure-velocity coupling *PISO* logarithm were employed for time integral and momentum balance as outlined in Issa [31]. The turbulent intensity at the inlet boundary condition was 2%, similar to the experimental method employed by Lyn and Rodi [32] and Mizukami [33]. The instability-induced motion is derived from Newton's law of motion, defined by the schematic of Figure 1 below.

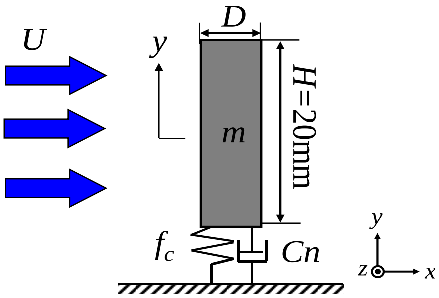

Fig. 1. The schematic of one DoF fluid-prism interaction

The instability-induced motion was calculated using the equation of motion of one degree of freedom, as shown in Eq. (6) to Eq. (11).

$$m\ddot{y} + c\dot{y} + ky = F_y \tag{9}$$

$$c = 2m\delta \frac{U}{V_r H} \tag{10}$$

$$k = 4\pi^2 m \left(\frac{U}{V_r H} \right)^2 \tag{11}$$

where c and k are the fluid damping and spring stiffness constants, respectively. For convenience, the equation of motion subsequently was discretized to cater governing components, i.e., acceleration, velocity, and displacement. The initial velocity of the prism displacement was set as $dy/dt = A\omega_c (A = 0.1H)$, where A, ω_c, and H denote the amplitude, angular frequency, and prism's height normal to the flow stream, respectively. The temporal solution of the ordinary differential equations was solved by the explicit method of the Adams-Bashforth multi-time step. The Adams-Bashforth predictor-corrector was verified for convergence and stability as in the study by Mizukami [33]. Therefore, second-order accuracy is adopted in this study.

2.1 Computational Domain

The schematic model of the computational domain of the cantilevered rectangular prism is shown in Figure 2. The finite rectangular prism with a cross-section height (*H*) normal to the flow stream is 20 mm, depth (*D*) of 10 mm, and span lengths variation (*L*) of 50, 100, 150, and 200 mm. A three-dimensional O-grid domain was developed with a diameter of 40*H*. The total number of grid points is a maximum of 4.41×10^6 with a minimum grid width of $5 \times 10^{-3}H$. The Reynolds number of 2.2×10^4 is employed in this study. The no-slip condition was applied at the prism and wall surface, and then the symmetry plane or frictionless wall was adopted at the bottom and top surfaces of the domain.

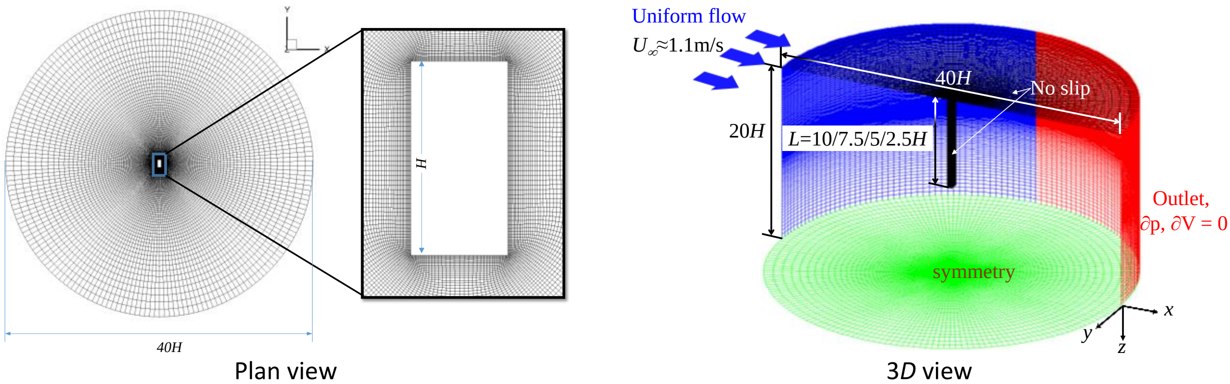

Fig. 2. Computational domain

2.2 Model Validation and Verification

The grid configuration was determined by considering the first cell height and growth rate of the mesh construction, which is determined by considering eddy motions at the viscous sublayer ($y^+<5$). The result showed that the y^+ calculation was 2.1, with the maximum value around 7.0. The value of y^+ considers the viscous stress linear to the wall distance. It shows a good agreement with the initial y^+ calculation as outlined in the studies by Versteeg and Malalasekera [34] and Kajishima and Taira [35]. The residual and mass balance were monitored for convergence criterion as outlined by Oberkampf and Trucano [36] and Oberkampf and Barone [37].

The flow feature around the infinite rectangular prism was analyzed first and then extended to the finite model with a similar method. The flow features or global quantities comparison of flow past the slender prism are shown in Table 1. The drag and base pressure coefficient are sensitive to the side ratios (*D/H*) variation, where the depth *D* =~0.6 *H* is the critical depth [42]. The Strouhal number of the rectangular prism with $D/H \leq 1.0$ is less sensitive than the hydrodynamics forces. The infinite prism's drag and base pressure coefficients agree with other numerical calculations and slightly differ from the experimental investigations. The Strouhal frequency is also reasonable, in agreement with both numeric and experimental studies. However, the finite prism presents different flow characteristics from the infinite model that the global quantities are sensitive to the presence of the end tip.

Table 1
The flow quantity parameters for the rectangular prism with a side ratio of 0.5

		CD (= $\frac{F_D}{0.5\rho \cdot U^2 H \cdot L}$)	St(= $\frac{U \cdot H}{f_w}$)	-Cpb(= $\frac{P}{0.5\rho \cdot U^2}$)	Re(= $\rho\frac{U}{\mu \cdot H}$)	Remark
Tamura and Itoh [38]	Simulation	2.81	0.13		10000	*2.5D Infinite*
Haque *et al.,* [39]	Simulation	2.39		1.67	22000	*2.5D infinite*
Knisley [40]	Experiment	2.33	0.14		22000	infinite
Nakaguchi [15]	Experiment	2.5		1.29	2~6×10^4	*Infinite*
Hiroaki [41]	Experiment	2.46	0.13	1.74	38000	*Infinite*
Mizukami [33]	Simulation	2.84	0.132	2.33	22000	*2.5D LES Infinite*
Barata *et al.,* [11]	Simulation	2.80	0.14	2.40	22000	*2.5D LES Infinite*
Present	Simulation	1.4 – 1.5	0.11	0.6 – 0.66	2.2×10^4	*LES Finite*

3. Results and Discussion

Figure 3 shows the local vortex region of the rectangular prisms with aspect ratios (*L/H*) of 10 and 2.5. The flow structure is recognized for the tip end, von Karman, and base swirling vortex at the prism with an aspect ratio (*L/H)* of 10. The fluid separation point is located at the leading edge, a common feature of the prismatic body with a sharp edge. A Sheared flow from the tip end immediately induces a downwash flow to merge to a spanwise vortex or regular Karman vortex. For the short prism (*L/H* = 2.5), the tip-end vortex dominates the flow structure and diminishes the spanwise vortex. The base and symmetrical horseshoe vortex formations are recognized at the ground. The horseshoe vortex is not sensitive to the aspect ratio for all test models (*AR* = 10 – 2.5) and is still recognized at the slender prism. These data are consistent with experimental findings studied by Sumner *et al.,* [43]. The downstream horseshoe vortex existence is also presented by Rastan *et al.,* [44]. The helical vortex induced by the base and tip-end vortices is clearly seen further downstream of the prism with *L/H* = 2.5, which is considered to replace the regular Karman vortex downstream. The arch-type vortex is located at the prism's base. The free-end absence of the finite-length prism provides a strong spinning local vortex at the trailing edge (see Figure 3(c)). It is considered to affect the fluid force quantities shown in Figure 4.

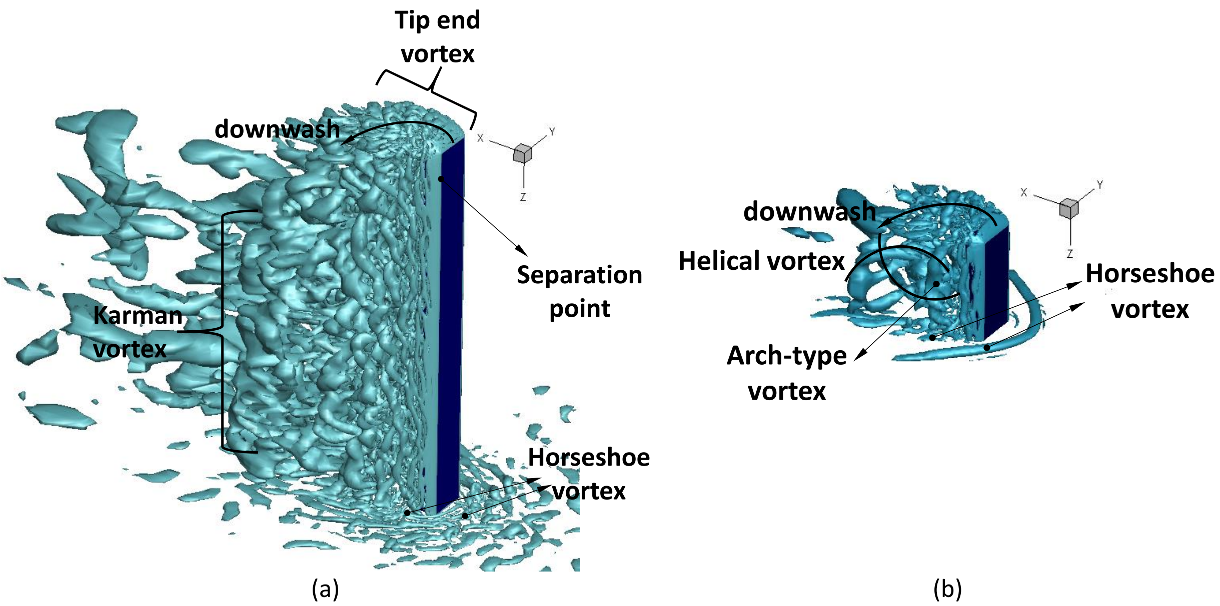

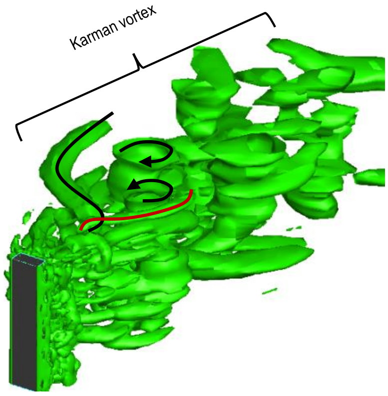

(c)

Fig. 3. The spanwise local vortex region on the finite length rectangular prisms; (a) *L/H* = 10, (b) *L/H* = 2.5. (c) The spinning Local vortex region in the infinite length rectangular prism (adopted from Barata *et al.,* [11])

3.1 Fluid Forces

Figure 4 presents the variation of the fluid force components for the finite and infinite prism. All the parameters were taken at the prism's mid-length to avoid the effect of the base or tip swirling vortex. The infinite prism (2.5D) exhibited a base pressure and drag coefficient larger than the 3D prism. It implies that the end tip condition influences spanwise vortex behavior, which is a flow structure of the prism's base. Decreasing the base pressure along the span length reduces the drag force component, which correlates to the sheared layer separation at the side surface of the prism. The wake fluctuation frequency of the 3D prism is weaker than the infinite or 2.5D model (see also Figure 3). However, increasing the span length (*L/H*) slightly increases the frequency of vortex shedding at the prism streamwise, as indicated in Figure 4. The velocity component (*u*) fluctuation was also confirmed by calculating the lift fluctuation. This phenomenon is similar to the circular cylinder studied by Kawamura *et al.,* [45]. The fluid force components from studies of the slender rectangular prism are presented in Table 1. The Strouhal frequency along the prism spanwise is presented in Figure 5. The fluctuation velocity vector was measured at *4H* and *1H* in downstream and transverse points, respectively. It is consistent with the method suggested by Tamura and Dias [46]. The lift fluctuation calculation's result confirmed the velocity fluctuation at the mid-span. Near the prism's tip, the fluctuation component weakens, which suggests the contribution of the presence of the end tip. Unsymmetrical vortices likely exhibit their existence near the end tip. A weakened fluctuation is recognized along spanwise of the *AR* = 2.5, and no clear peak frequency at the selected span's planes. It suggests that turbulence intensity is lower than its counterparts. In the case of the slender prismatic body of rectangular prisms, the fluctuation frequency is not sensitive with respect to the aspect ratio, mainly for *AR* ≥ 2.5.

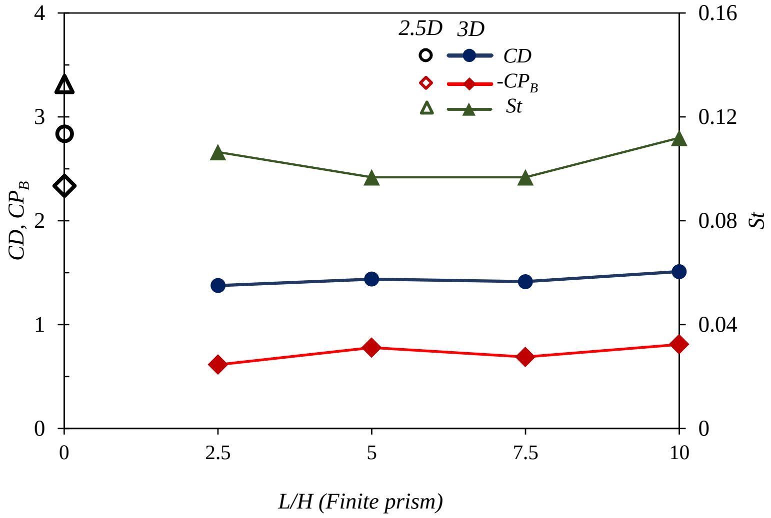

Fig. 4. Effect of the span lengths variation on the hydrodynamic force components

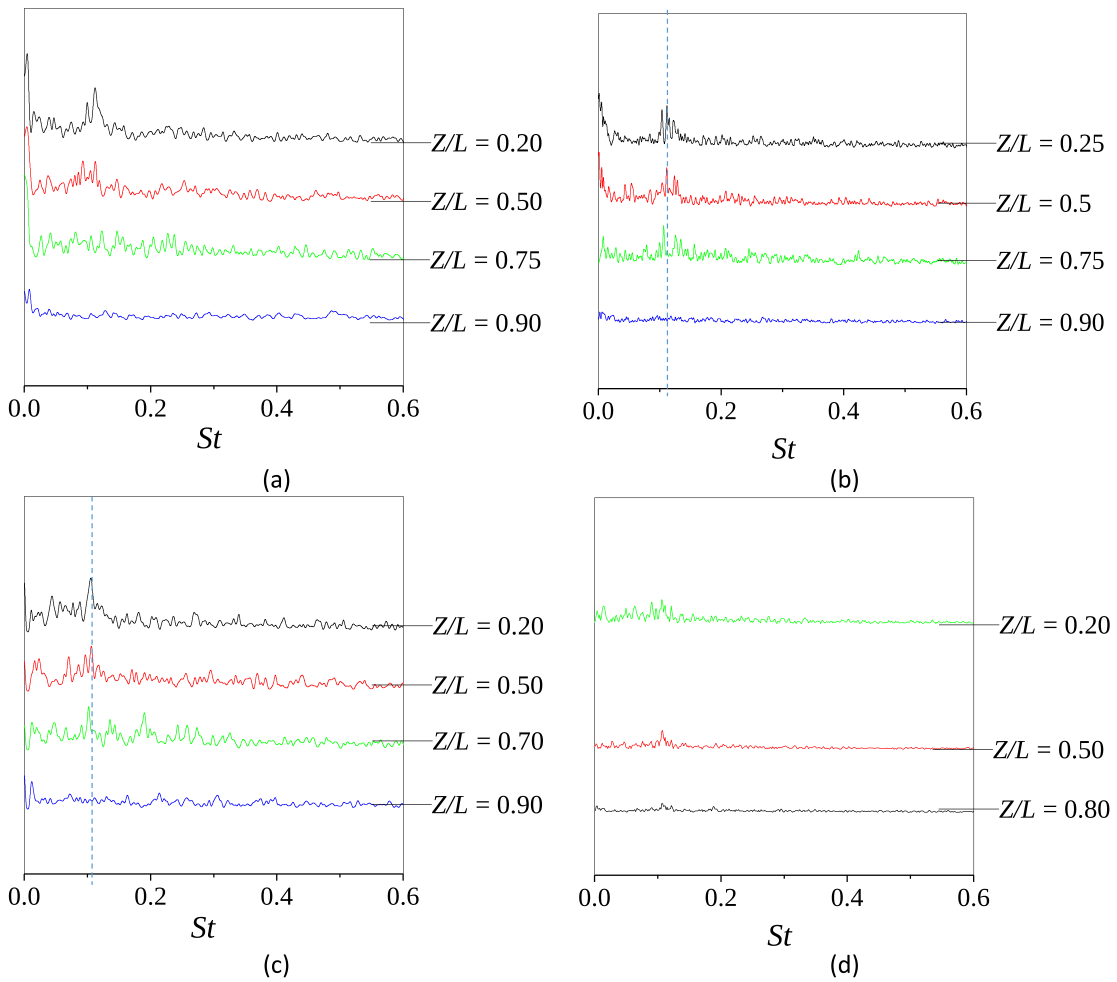

Fig. 5. Flow stream fluctuation around the bluff body at various the span planes (*Z/L*); (a) AR = 10, (b) AR = 7.5, (c) AR = 5, (d) AR = 2.5

3.2 Velocity Vector

Figure 6 presents the velocity vector distribution along the streamwise positions at the prism's mid-plane. The velocity profile at the prism's trailing edge (*X/H* = 0.5) shows different behavior from the downstream *u*-component because of the bubble's effect. The separated sheared layer at the side surfaces induces fluid to accelerate to a *2H* streamwise position, and the viscous boundary is clearly defined. The negative base pressure in the viscous layer causes potent flow entrainment at the prism's base, which is indicated by reserved flow at the prism's vicinity. The reserved flow length descends by increasing the downstream flow regime. The velocity vector deformation effect varies with the *x*-coordinate position.

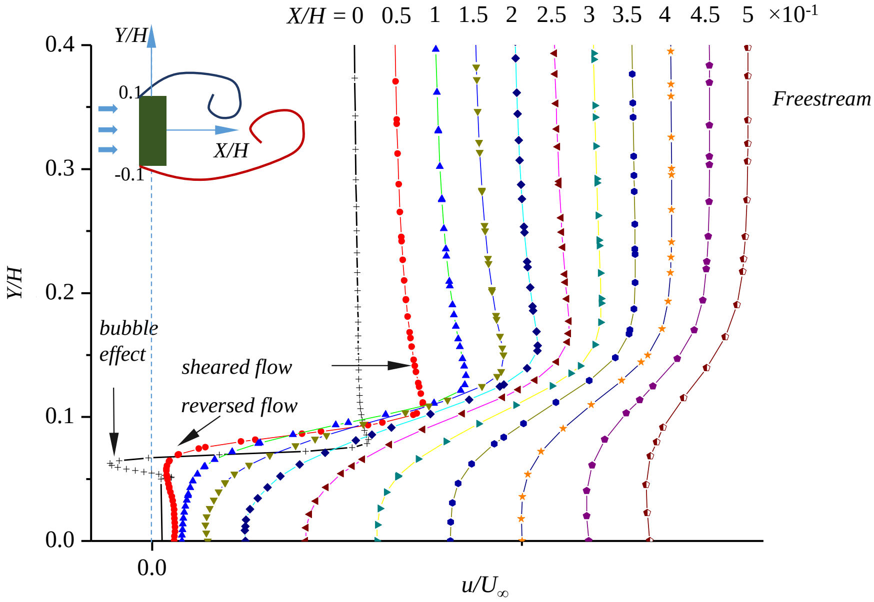

Fig. 6. Streamwise mean velocity profile with respect to the transverse direction for *L/H* = 2.5

Figure 7 shows the mean velocity vector distribution at various span lengths with respect to the downstream locations. The effect of the separated shear layer from the end tip on the velocity distribution is absent at the mid-plane of *L/H* = 10. Moreover, the velocity (*u*-component) profile at the midplane is similar to the wall boundary (top boundary condition) with a no-slip condition.

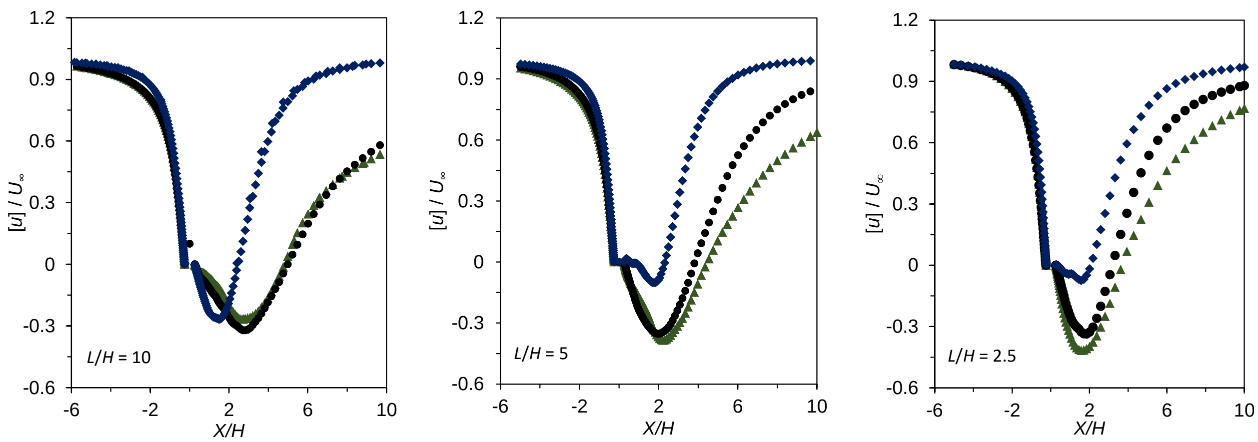

Fig. 7. Normalized velocity vector profile at the *Z*-planes variation

The reversed flow intensity near the tip (*Z/L* = 0.9) descends for the prism with *L/H* ≤ 5.0, while it is more negative at *Z/L* = 0.5. The upwash effect dominates the spanwise vortex (see Figure 8(b)), so the velocity profile near the tip distinctly differs from the prism with *L/H* = 10. The velocity profile at the mid-spanwise (*Z/L* = 0.5) tends to approach the flow near the end tip at *X* > 4*H* locations. The steepness of the velocity profile at mid-plane slightly increases by reducing the aspect ratio. Far from the prism (at least *X* = 6*H*), the upwash effect (induced by the tip's separated layer) weakens at *L/H* = 10, which is different from *L/H* ≤ 5.0.

Figure 8(a) shows vorticity variation along the prism's spanwise (three different planes, *Z/L*), i.e., near the wall (top boundary condition), mid-plane, and near the prism's tip. It can be observed that the vorticity's width shrinks at the tip's vicinity. The *x*-mean velocity distribution at the span's mid-plane (*Y*=0) is presented in Figure 8(b). The center of recirculation (*CR*) is located immediately at the prism's end tip, induced by the separated shear layer from the end tip (bubble effect). Further, the secondary *CR* is located at the base, followed by the negative velocity area. The secondary *CR* position shifts away from the end tip by reducing AR for *AR* ≤ 5.0. The existence of secondary *CR* at the base is also enclosed between the separated shear layer from the tip and the negative span area. The downstream reversed flow (*XR*) length is typically around 4*H*. This area is bounded by the stagnation borderline (*SB*) where stagnation velocity exists. It is noted that *SB* varies with the prism's span coordinate with respect to the downstream position. *SB* line from downwash slack at the critical point (saddle point, *SP*) where upwash meets at the point. The saddle point tends to approach the base by reducing *AR*. It is consistent with the experimental data studied by Sumner *et al.,* [43].

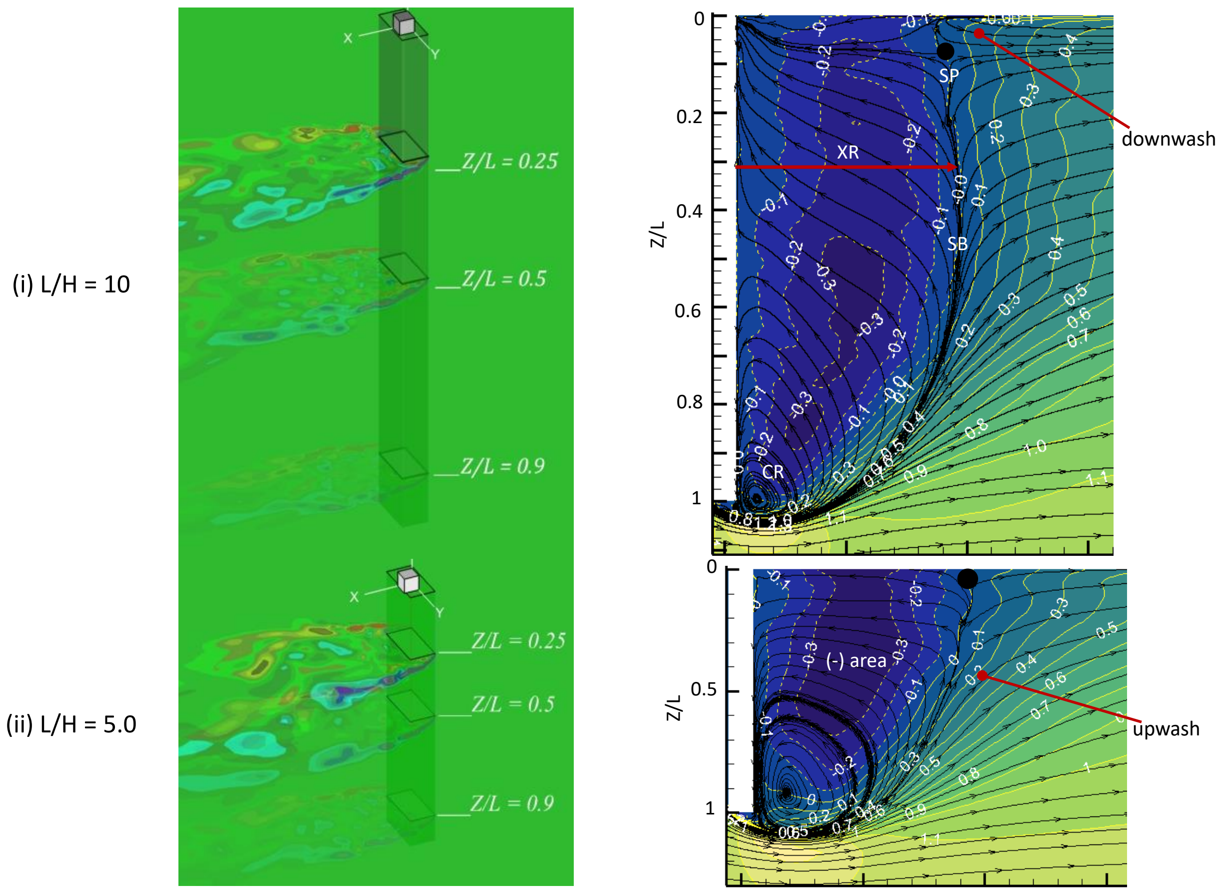

(iii) L/H = 2.5

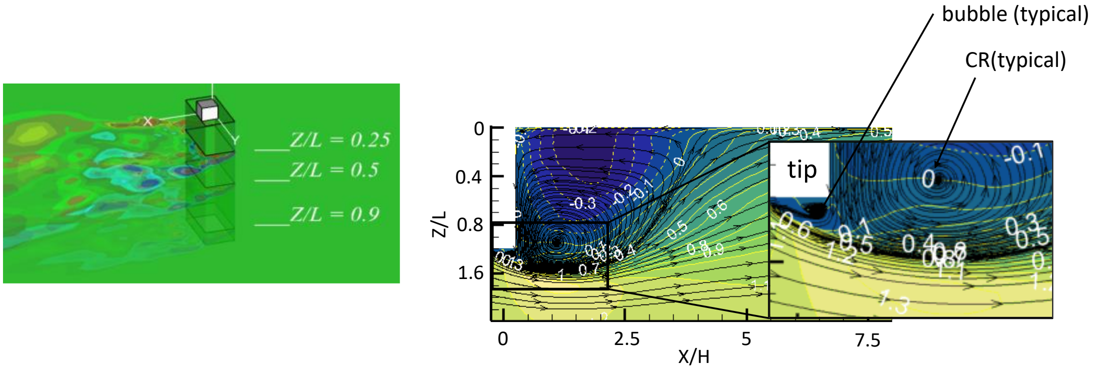

(a) (b)

Fig. 8. (a) The spanwise vorticity at various *Z*-planes for the rectangular prisms with different aspect ratios *L/H* (=10, 5.0, and 2.5). (b) The mean velocity vector at the mid vertical plane (*Y* = 0) which is featured by velocity contour scale behind for various aspect ratios *L/H* (=10, 5.0, and 2.5)

3.3 Reynolds Stress Components

The Reynolds normal stress components (u'^2, v'^2, and w'^2) for incompressible flow are presented in Figure 9 and Figure 10. For brevity's sake, Figure 9 and Figure 10 only show the Reynolds normal stress components along the prism's span of *AR* = 5 and 2.5. Figure 9 presents the Reynolds normal stress components for several *Z*-planes with respect to the downstream positions. Generally, the peak of turbulence shrinks near the end tip and moves close to the prism. The peak of streamwise normal stress [$u'u'$] near the tip of *AR* = 2.5 is slightly higher than that of the mid-plane (*Z/L*=0.5). It confirms that the interference of the end tip vortex to the spanwise vortex diminishes the regular Karman vortex. It is also confirmed in Figure 5. The peak shrinkage of the streamwise normal stress [$u'u'$] indicates the reduction of the bubble region. Similarly, it is also found in the transverse normal stress [$v'v'$] and spanwise normal stress [$w'w'$] components. Reynolds normal stress variations along the spanwise with respect to the downstream positions are presented in Figure 10. A dominant peak of streamwise normal stress is observed near the tip region, both *AR* = 5 and 2.5, due to the separated shear layer from the prism's tip. However, it is not found in transverse ($v'v'$) and spanwise ($w'w'$) normal stress. The intensity of streamwise, transverse, and spanwise normal stress is decreased with respect to the downstream locations for both aspect ratios (*AR*).

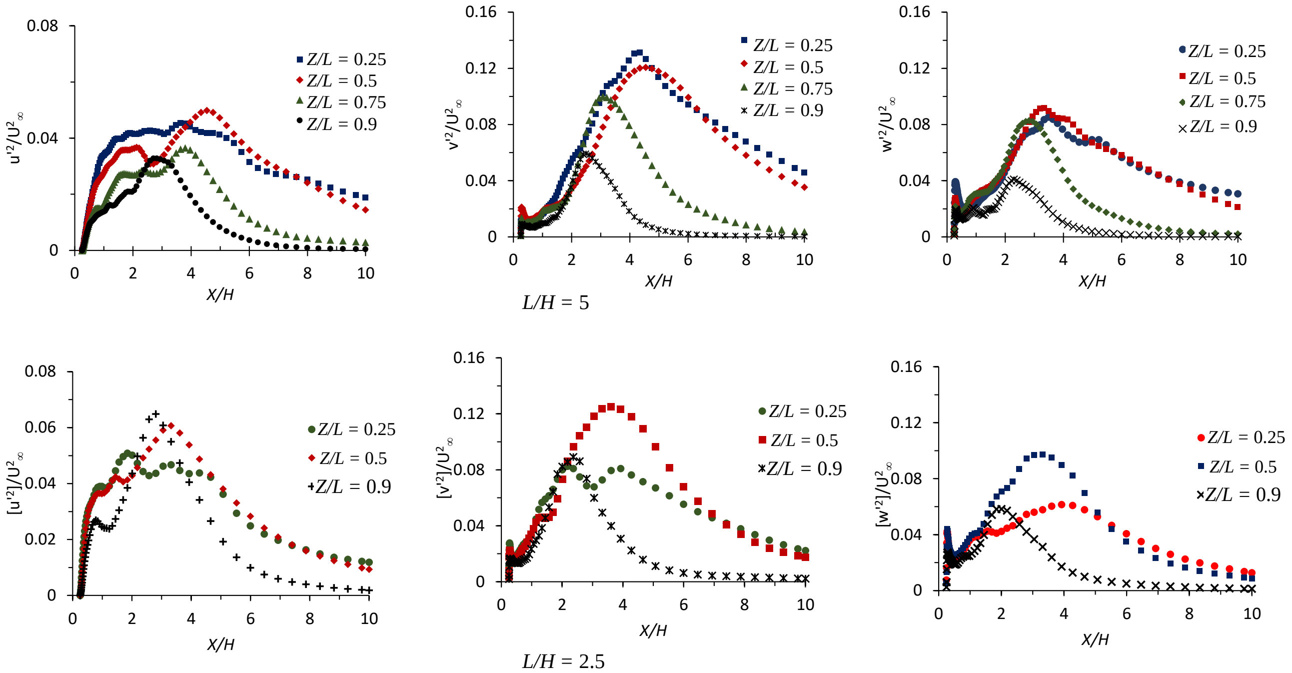

Fig. 9. Variation of the streamwise Reynolds normal stress components along the prism's span

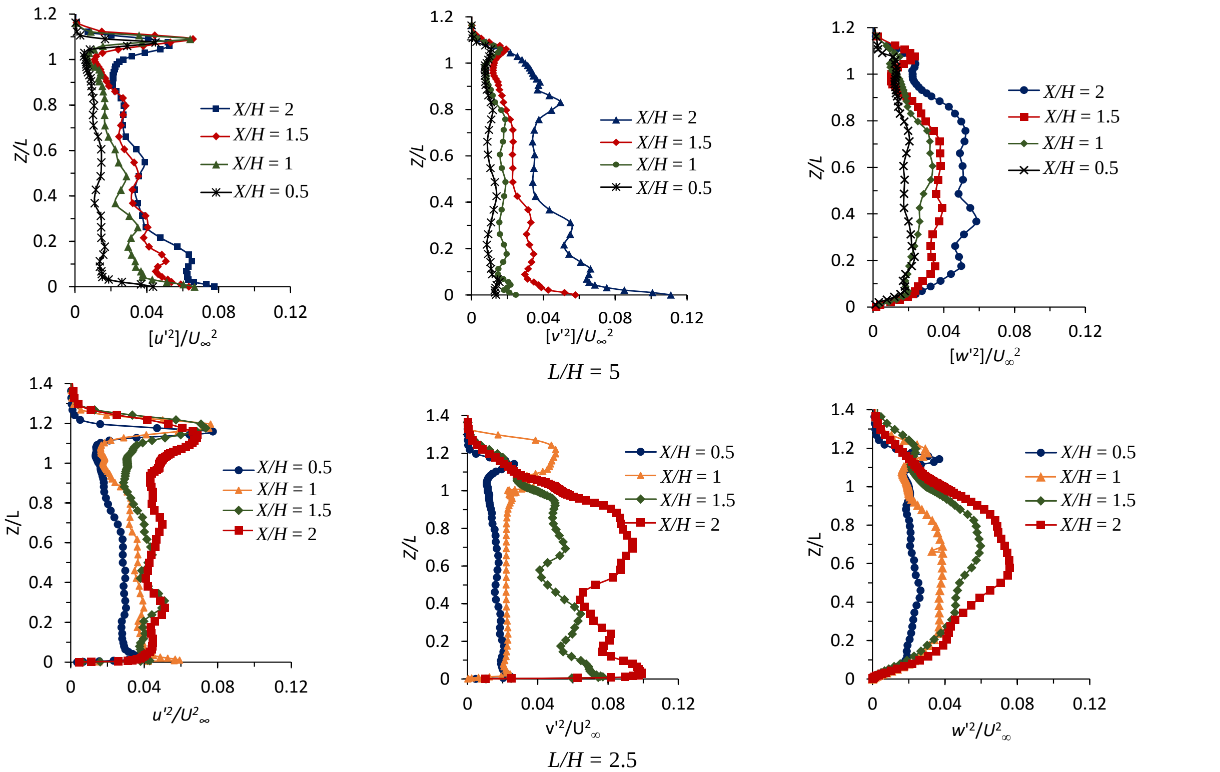

Fig. 10. Spanwise Reynolds normal stress components at the downstream positions

The shrinkage of Reynolds shear stress near the tip-end is also observed, as indicated in Figure 11. The peak of Reynolds shear stress components with respect to downstream locations is far from the prism. The momentum flux at the prism with *AR* = 2.5 is larger than *AR* = 5, which indicates energy transported is large.

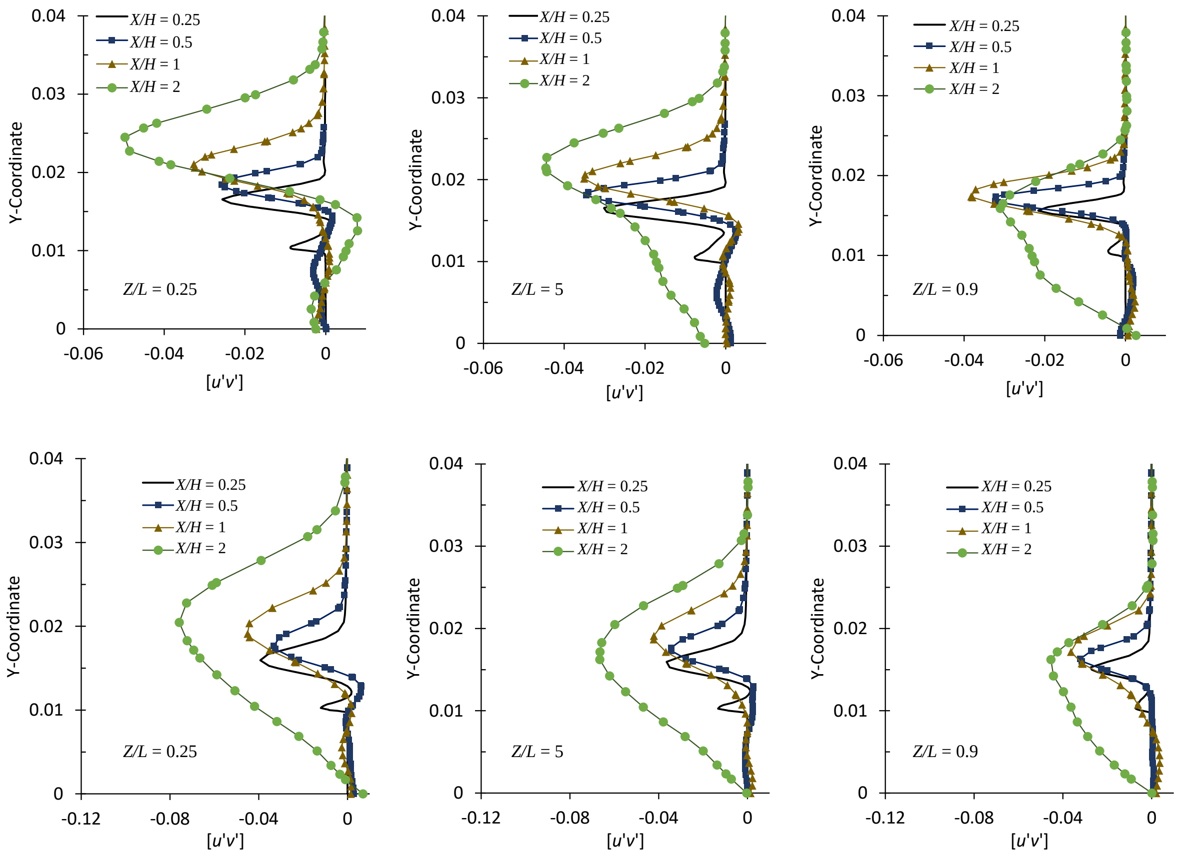

Fig. 11. Spanwise Reynolds shear stress components at the downstream locations

3.4 Pressure Field Components

The base pressure distribution along the prism's span length is shown in Figure 12(a). Span length variation affects the base pressure distribution, where the tip end area is the lowest pressure among the flow field. It implies that potent flow entrainment is typically located near the tip end, mainly for *AR*=10. Reducing the prism's span length recovers the base pressure mainly near the end tip. It can be said that flow entrainment at the tip's vicinity descends. The section view of pressure contours taken at the prism's midplane of $Z = 0.5\ L$ is shown in Figure 12(b). The most negative base pressure area shrank by reducing the aspect ratio (*AR*). The center of flow recirculation (*CR*) is typically not changed for $L/H \geq 5$, as mentioned in the previous section. However, the critical point or saddle point (*SP*) descends by reducing the aspect ratio (*AR*).

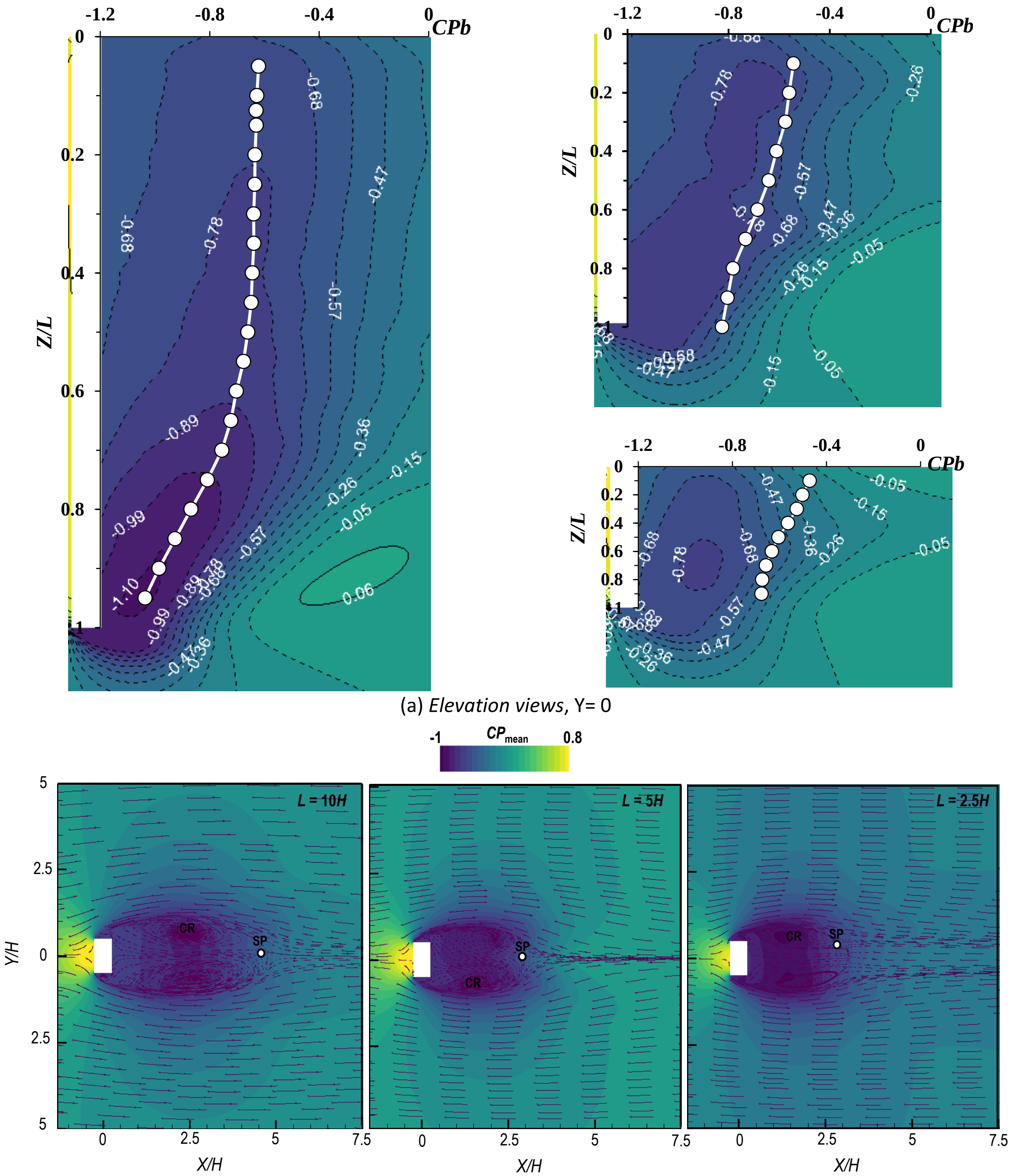

Fig. 12. (a) The mean base *CP* distribution which is featured mean CP contour at vertical mid-plane (*Y* = 0), and (b) Mid plane of the mean pressure contours which is featured by velocity vector component (Z = 0.5*L*)

Figure 13 presents the pressure distributions along the prism span length at various section planes. The pressure distribution at the side and base surfaces shows similar characteristics that are varied regularly along the span length. The alteration of base pressure along the prism's span indicates the level of the downwash/upwash flow effect. Meanwhile, the pressure profile at side surfaces is attributed to the bubble effect induced by the separated shear layer from the prism's leading edge. The prism with *AR* ≥ 5.0 shows a similar pressure profile near the tip end (*Z/L* = 0.75) with more negative pressure than other span positions (note that the pressure profile at the tip, *Z/L* = 1, is omitted). However, pressure distribution at the prism near the end tip for *AR* ≤ 5.0 show a distinctive pressure profile that indicates flow structure change of *AR* ≤ 5.0 with respect to the end tip end effect. The investigations on the end tip effect suggest the critical length with respect to the cross-section height or diameter is *AR* = ~3.0. [45,47].

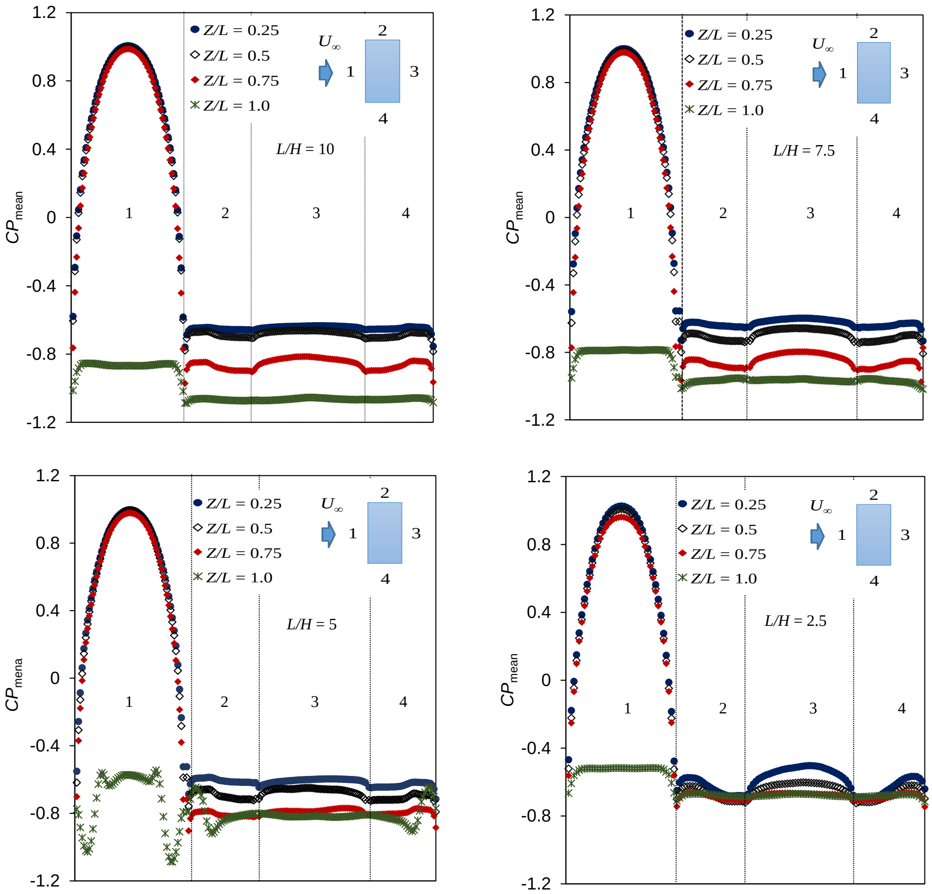

Fig. 13. The mean pressure coefficient profiles at the prism's surfaces along the span

3.5 Instability-Induced Motion

The predicted transverse motion of the prism with respect to non-dimensional velocity is presented in Figure 14. The non-dimensional parameter of the prism's vibration is defined by a reduced velocity V_r (= $U_\infty/f_c \times H$) where U_∞ is the flow stream velocity, f_c and H denote frequency characteristic and cross-section height of the prism, respectively. A comparison from experimental data was taken from Barata *et al.,* [48], which measured the tip displacement of a cantilevered type slender rectangular prism (*D*= 0.5*H*). Mizukami *et al.,* [49] compared the 2.5D predicted motion of a rectangular cylinder to experimental data of a cantilevered rectangular prism. Predicted transverse motion of the prism typically showed a good agreement at low reduced velocity ($V_r \leq 4$). In this case, V_r calculation was only taken up to V_r = 5, which shows a deviation from the experimental at Vr > 4.

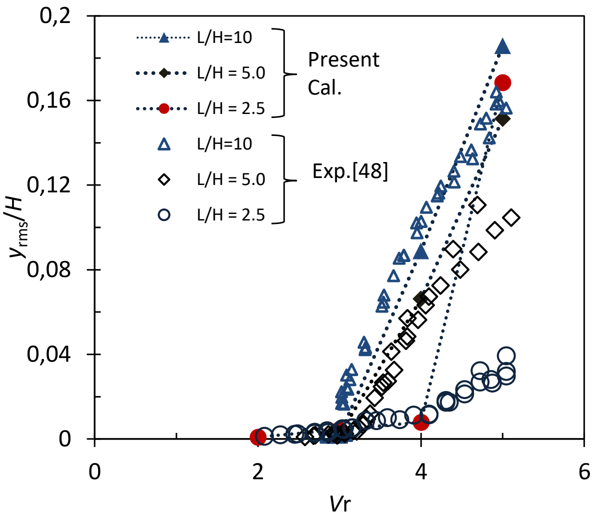

Fig. 14. Prism's dynamic response with respect to non-dimensional velocity

Figure 15 presents the effect of the prism's dynamic response on the mean base pressure profile. Overall, base pressure is sensitive to the prism's dynamic response intensity, which vibrating prism induces the base pressure to be more negative along the prism's span than the stationary prism. However, the base pressure increase near the prism's tip, which suggests the prism's motion reduces the bubble effect at the prism's downstream. In contrast, far from the tip or (*Z/L* =~ 0.5), the prism's dynamic response induces the base pressure to be more negative (see vorticity contours in Figure 18).

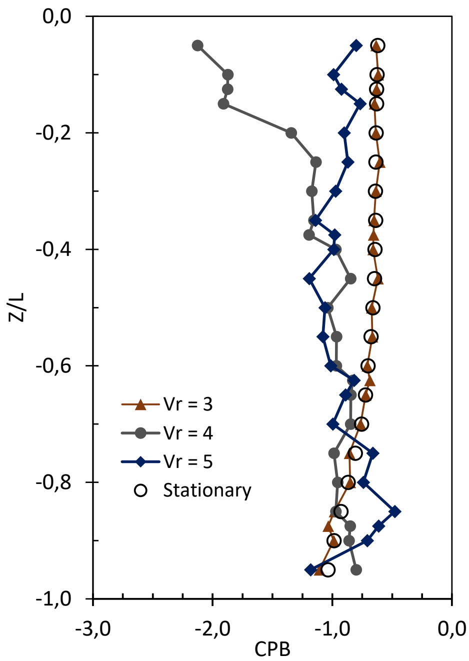

Fig. 15. The span mid plane (Y = 0) of the mean base pressure coefficient variation along the span length of stationary and vibrating prisms with AR = 10

Figure 16 compares time histories of *CL* component and prism dynamic response, while *FFT* spectra of frequencies are shown downward in Figure 16. Both the *CL* component and the prism's dynamic response are synchronous. *FFT* spectra of vibration response frequency (f_y) were calculated based on velocity vector fluctuation at the prism downstream, as outlined in the previous section. The primary peak of wake fluctuation (f_w) is different from vibration frequency, both *L/H* = 10 and 5. It is a common feature of instability-induced motion of rectangular prism with an aspect ratio less than critical depth (=$D \leq 0.67H$). The studies related to this characteristic can be found in researches by Barata *et al.,* [11], Nakamura and Hirata [42], Ohya [50], etc. A secondary peak vibration fluctuation also locked in wake fluctuation for both prism models, as shown in Figure 16. Barata *et al.,* [11,51] presented that fully synchronous vibration frequency occurs at high amplitude response where the secondary peak of vibration FFT spectra vanishes. It implies that the vibration motion alters the flow structure in the wake (see Figure 18(b)).

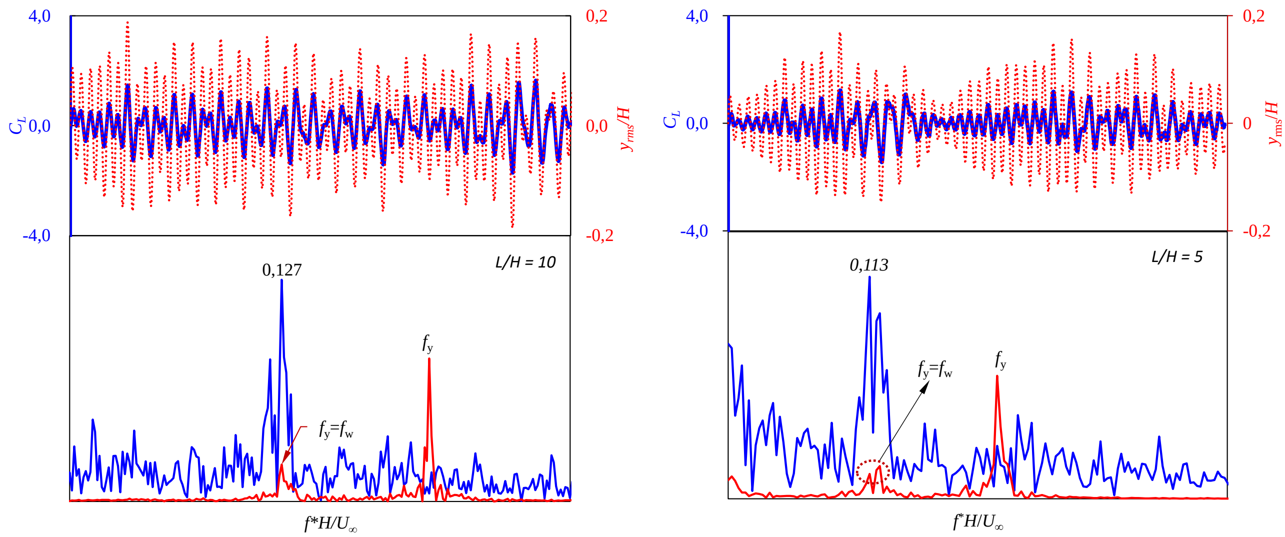

Fig. 16. Time histories of lift force and prism dynamic response (upper), and FFT spectra of frequencies (bottom) at V_r = 4

The effect of vibration response on the flow quantities is presented in Figure 17. Drag (*CD*) and base pressure coefficient (*CPB*) components changed with V_r variation, while Strouhal frequency exhibited a small change for AR ≥ 5.0. Moreover, *CD* fluctuation is more sensitive to V_r variation, which suggests a significant deviation in high reduced velocity (V_r). The contribution of the end tip effect on the flow quantities alteration is clearly shown at *AR* = 2.5, where all flow quantities descended with respect to V_r variation.

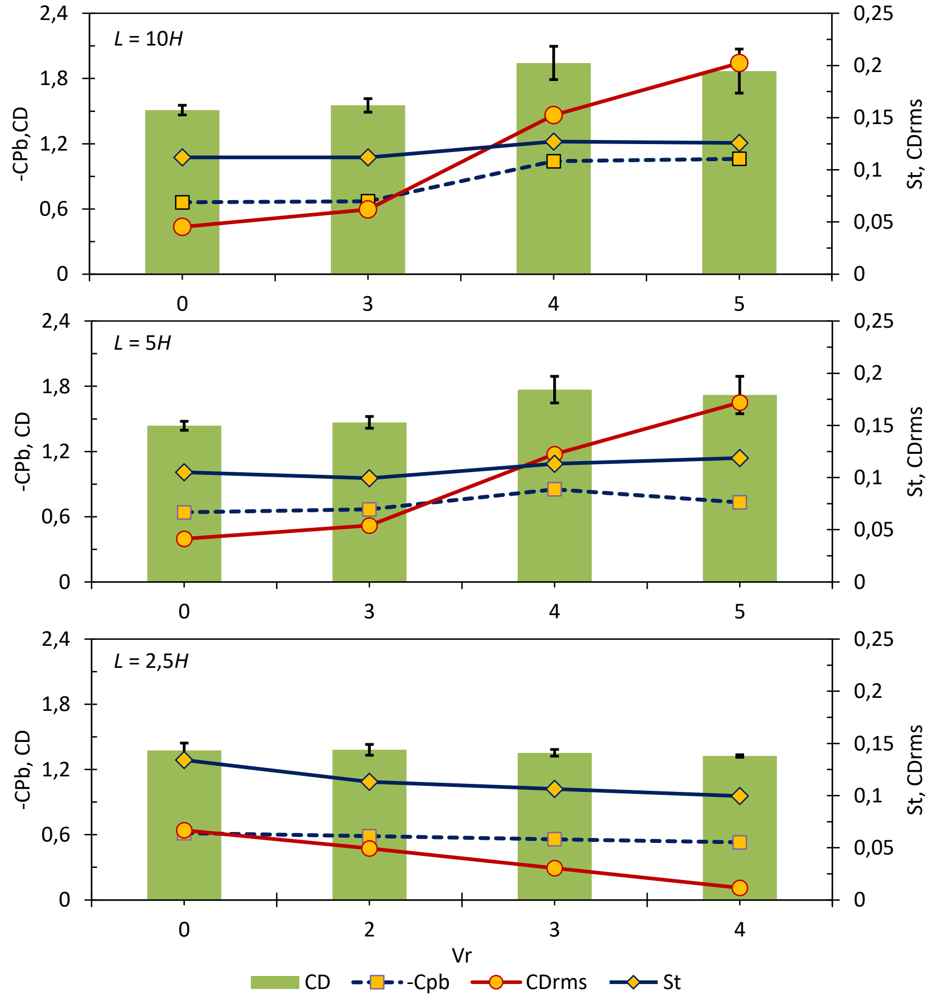

Fig. 17. Flow quantities of the prisms model with various vibration intensities

The effect of V_r variation on the flow field characteristics is shown in Figure 18. The symmetrical vortices can be observed at the stationary prism along the span length planes (see Figure 18(a)). Distinctive flow patterns appear in the vibrating prism along the span-length planes that exhibit unsymmetrical flow patterns. The level of the swirling vortex at the base is dependent on V_r. The contribution of the end tip effect can be observed in that negative vorticity descend near the tip-end, and the swirling negative vortex is seen at the mid-plane (Z/L = 0.5). Shrinkage of the recirculation bubble region is clearly shown at vibrating prism vorticity contours. The global fluid force quantity, such as the drag coefficient, shows significant fluctuation at a high vibrating prism (V_r= 4), as confirmed in Figure 17.

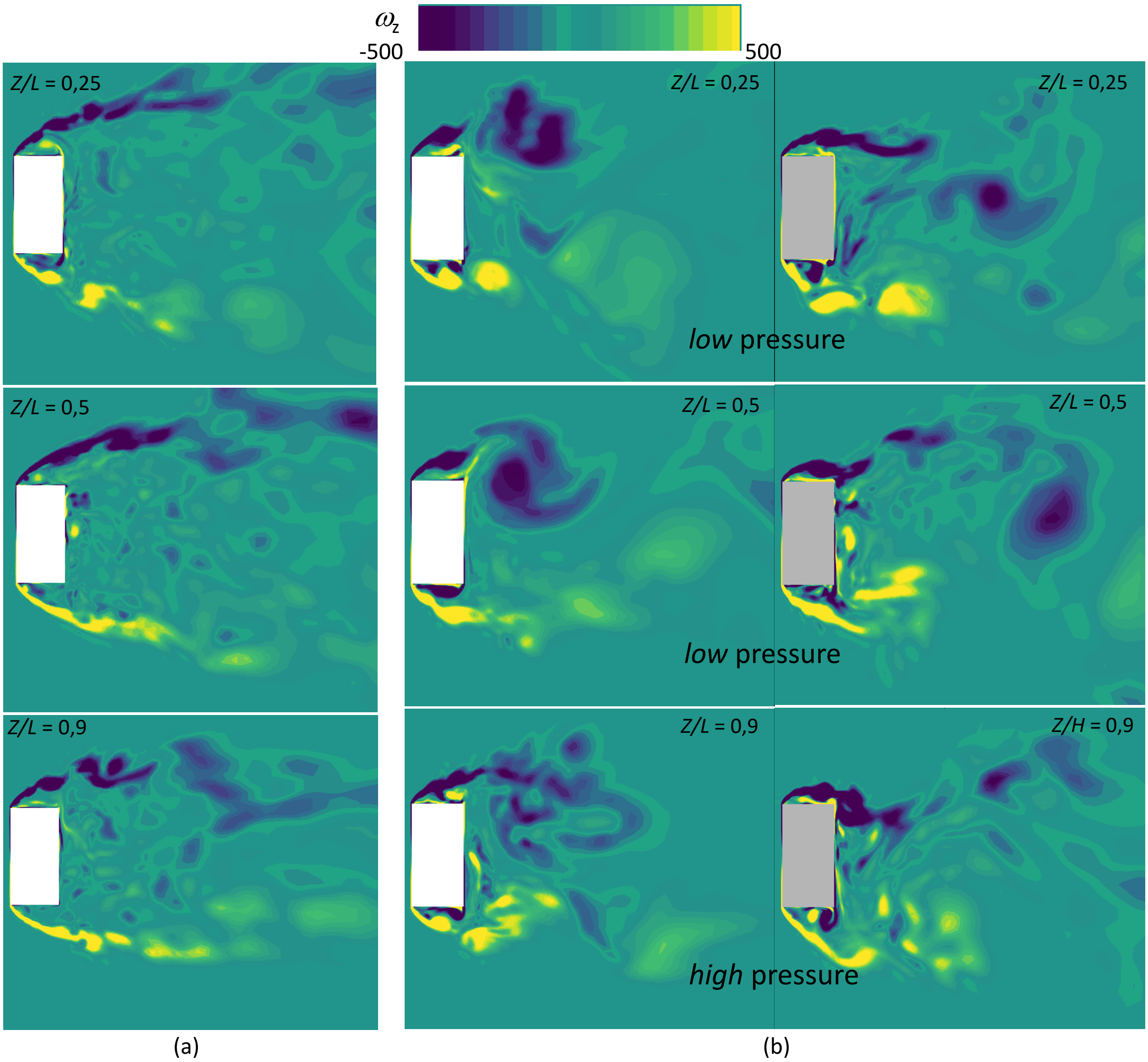

Fig. 18. Vorticity contours profile at various prism's span planes (*Z/L*). (a) Stationary state for the prism with *L* = 10*H*, (b) Vibrating prism at *Vr* = 4,0 for the prisms with *L* = 10*H,* and *L* = 5*H*

4. Conclusions

3D Large Eddy Simulation turbulence model was used to investigate the flow features around the slender rectangular prism with cross-section height (*H*) to streamwise depth (*D*) ratio or side ratio (*D/H* = 0.5) with Reynolds number Re = 22000. The presence of the end tip alters the flow features, which is indicated by the alteration of global quantities such as drag, non-dimensional frequency, and base pressure coefficient components. The global quantities of the 3D slender prism are different from the 2D prism, suggesting the flow structure difference between them. The effect span length variation on the flow features unveiled the flow structure change on 3D slender rectangular. It implies that the 3D flow structure changes at *L* < *5H*, where the separated shear layer for the tip end diminishes the regular Karman vortex and reduces the vorticity area. The flow features of the vibrating prism showed distinctions compared to the stationary structure. The effect of the vibrating prism on the flow structure exhibited potent entrainment at the base where the base pressure is low. However, it did not occur near the tip-end (*Z/L* =~ 0.9), where the base pressure increased at V_r = 5.

Acknowledgment
CFD code was carried out using the HPC workstation Fluid Dynamics Laboratory, Kanazawa University JAPAN, under the authors' collaborative works agreement. The authors thank Dr. Sunichi Mizukami for his valuable support in CFD works. This research was not funded by any grant.

References

[1] Sakamoto, S., S. Murakami, S. Kato, and A. Mochida. "Unsteady pressure field around oscillating prism predicted by LES." *Journal of Wind Engineering and Industrial Aerodynamics* 46 (1993): 551-556. https://doi.org/10.1016/0167-6105(93)90322-F

[2] Bearman, Peter W. "Vortex shedding from oscillating bluff bodies." *Annual Review of Fluid Mechanics* 16, no. 1 (1984): 195-222. https://doi.org/10.1146/annurev.fl.16.010184.001211

[3] Blevins, Robert Dilworth. "Flow induced Vibrations of Bluff Structures." *PhD diss., California Institute of Technology*, 1974.

[4] Billah, K. Yusuf, and Robert H. Scanlan. "Resonance, Tacoma Narrows bridge failure, and undergraduate physics textbooks." *American Journal of Physics* 59, no. 2 (1991): 118-124. https://doi.org/10.1119/1.16590

[5] Zdravkovich, M. M. "Modification of vortex shedding in the synchronization range." *ASME Journal of Fluids Engineering* 104, no. 4 (1982): 513-517. https://doi.org/10.1115/1.3241895

[6] Griffith, Martin D., David Lo Jacono, John Sheridan, and Justin S. Leontini. "Flow-induced vibration of two cylinders in tandem and staggered arrangements." *Journal of Fluid Mechanics* 833 (2017): 98-130. https://doi.org/10.1017/jfm.2017.673

[7] Ding, Lin, Li Zhang, Eun Soo Kim, and Michael M. Bernitsas. "URANS vs. experiments of flow induced motions of multiple circular cylinders with passive turbulence control." *Journal of Fluids and Structures* 54 (2015): 612-628. https://doi.org/10.1016/j.jfluidstructs.2015.01.003

[8] Kim, Sangil, and Md Mahbub Alam. "Characteristics and suppression of flow-induced vibrations of two side-by-side circular cylinders." *Journal of Fluids and Structures* 54 (2015): 629-642. https://doi.org/10.1016/j.jfluidstructs.2015.01.004

[9] Chauhan, Manish Kumar, Sushanta Dutta, Bhupendra Singh More, and Bhupendra Kumar Gandhi. "Experimental investigation of flow over a square cylinder with an attached splitter plate at intermediate Reynolds number." *Journal of Fluids and Structures* 76 (2018): 319-335. https://doi.org/10.1016/j.jfluidstructs.2017.10.012

[10] Sharma, K. R., and Sushanta Dutta. "Flow control over a square cylinder using attached rigid and flexible splitter plate at intermediate flow regime." *Physics of Fluids* 32, no. 1 (2020): 014104. https://doi.org/10.1063/1.5127905

[11] Barata, La Ode Ahmad, Edward Ngii, Takahiro Kiwata, and Takaaki Kono. "Enhancing Dynamic Response of Cantilevered Rectangular Prism Using a Splitter Plate as a Passive Turbulence Control in Water Tunnel." *Journal of Advanced Research in Fluid Mechanics and Thermal Sciences* 91, no. 2 (2022): 1-14. https://doi.org/10.37934/arfmts.91.2.114

[12] Mashhadi, A., A. Sohankar, and Md Mahbub Alam. "Flow over rectangular cylinder: Effects of cylinder aspect ratio and Reynolds number." *International Journal of Mechanical Sciences* 195 (2021): 106264. https://doi.org/10.1016/j.ijmecsci.2020.106264

[13] Rostamy, N., D. Sumner, D. J. Bergstrom, and J. D. Bugg. "Local flow field of a surface-mounted finite circular cylinder." *Journal of Fluids and Structures* 34 (2012): 105-122. https://doi.org/10.1016/j.jfluidstructs.2012.04.014

[14] Gonçalves, Rodolfo Trentin, Guilherme Rosa Franzini, Guilherme F. Rosetti, Julio Romano Meneghini, and André Luis Condino Fujarra. "Flow around circular cylinders with very low aspect ratio." *Journal of Fluids and Structures* 54 (2015): 122-141. https://doi.org/10.1016/j.jfluidstructs.2014.11.003

[15] Nakaguchi, Hiroshi. "An experimental study on aerodynamics drag of rectangular cylinders." *Journal of the Japan Society for Aeronautical and Space Sciences* 16, no. 168 (1968): 1-5. https://doi.org/10.2322/jjsass1953.16.1

[16] Okajima, Atsushi, Kenichiro Sugitani, and Takehito Mizota. "Observation of flow around rectangular cylinders." *Journal of The Flow Visualization Society of Japan* 2, no. Supplement (1982): 71-74. https://doi.org/10.3154/jvs1981.2.Supplement_71

[17] Nakamura, Yasuharu, and Katsuya Hirata. "Critical geometry of oscillating bluff bodies." *Journal of Fluid Mechanics* 208 (1989): 375-393. https://doi.org/10.1017/S0022112089002879

[18] Bruno, Luca, Davide Fransos, Nicolas Coste, and Arianna Bosco. "3D flow around a rectangular cylinder: a computational study." *Journal of Wind Engineering and Industrial Aerodynamics* 98, no. 6-7 (2010): 263-276. https://doi.org/10.1016/j.jweia.2009.10.005

[19] Tian, Xinliang, Muk Chen Ong, Jianmin Yang, and Dag Myrhaug. "Unsteady RANS simulations of flow around rectangular cylinders with different aspect ratios." *Ocean Engineering* 58 (2013): 208-216. https://doi.org/10.1016/j.oceaneng.2012.10.013
[20] Liu, Y. Z., C. M. Ma, K. S. Dai, A. El Damatty, and Q. S. Li. "Improved understanding of transverse galloping of rectangular cylinders." *Journal of Wind Engineering and Industrial Aerodynamics* 221 (2022): 104884. https://doi.org/10.1016/j.jweia.2021.104884
[21] Wang, Chaoqun, Qing Wen, Shuai Zhou, Xugang Hua, Zhiwen Huang, and Zhengqing Chen. "Effects of end condition and aspect ratio on vortex-induced vibration of a 5: 1 rectangular cylinder." *Journal of Fluids and Structures* 109 (2022): 103480. https://doi.org/10.1016/j.jfluidstructs.2021.103480
[22] Pattenden, R. J., S. R. Turnock, and Xin Zhang. "Measurements of the flow over a low-aspect-ratio cylinder mounted on a ground plane." *Experiments in Fluids* 39 (2005): 10-21. https://doi.org/10.1007/s00348-005-0949-9
[23] Sumner, D., and J. L. Heseltine. "Tip vortex structure for a circular cylinder with a free end." *Journal of Wind Engineering and Industrial Aerodynamics* 96, no. 6-7 (2008): 1185-1196. https://doi.org/10.1016/j.jweia.2007.06.039
[24] Rostamy, Nooralllah, David Sumner, Donald J. Bergstrom, and James D. Bugg. "An experimental study of the flow above the free ends of surface-mounted bluff bodies." In *Fluids Engineering Division Summer Meeting*, vol. 44755, pp. 981-990. American Society of Mechanical Engineers, 2012. https://doi.org/10.1115/FEDSM2012-72028
[25] Palau-Salvador, Guillermo, Thorsten Stoesser, Jochen Fröhlich, Michael Kappler, and Wolfgang Rodi. "Large eddy simulations and experiments of flow around finite-height cylinders." *Flow, Turbulence and Combustion* 84 (2010): 239-275. https://doi.org/10.1007/s10494-009-9232-0
[26] He, Jia-wei, Wei-wen Zhao, De-cheng Wan, and Yi-qian Wang. "Numerical study of free end effect of cylinder with low aspect ratios on vortex induced motion." *Journal of Hydrodynamics* 34, no. 1 (2022): 106-115. https://doi.org/10.1007/s42241-022-0011-x
[27] Larsson, Johan, Soshi Kawai, Julien Bodart, and Ivan Bermejo-Moreno. "Large eddy simulation with modeled wall-stress: recent progress and future directions." *Mechanical Engineering Reviews* 3, no. 1 (2016): 15-00418. https://doi.org/10.1299/mer.15-00418
[28] Nicoud, Franck, and Frédéric Ducros. "Subgrid-scale stress modelling based on the square of the velocity gradient tensor." *Flow, Turbulence and Combustion* 62, no. 3 (1999): 183-200. https://doi.org/10.1023/A:1009995426001
[29] Tey, Wah Yen, Yutaka Asako, Nor Azwadi Che Sidik, and Goh Rui Zher. "Governing equations in computational fluid dynamics: Derivations and a recent review." *Progress in Energy and Environment* 1 (2017): 1-19.
[30] ANSYS. "Ansys Fluent 18.2 Theory Guide." *ANSYS Inc*., 2017.
[31] Issa, Raad I. "Solution of the implicitly discretised fluid flow equations by operator-splitting." *Journal of Computational Physics* 62, no. 1 (1986): 40-65. https://doi.org/10.1016/0021-9991(86)90099-9
[32] Lyn, D. A., and W. Rodi. "The flapping shear layer formed by flow separation from the forward corner of a square cylinder." *Journal of Fluid Mechanics* 267 (1994): 353-376. https://doi.org/10.1017/S0022112094001217
[33] Mizukami, S. "Study on the flow around the elastically supported prism and the vibration dynamics of the flow." *Master thesis, Kanazawa University*, 2017.
[34] Versteeg, Henk Kaarle, and Weeratunge Malalasekera. *An introduction to computational fluid dynamics: the finite volume method*. Pearson Education, 2007.
[35] Kajishima, Takeo, and Kunihiko Taira. *Computational fluid dynamics: incompressible turbulent flows*. Springer, 2017. https://doi.org/10.1007/978-3-319-45304-0
[36] Oberkampf, William L., and Timothy G. Trucano. "Verification and validation in computational fluid dynamics." *Progress in Aerospace Sciences* 38, no. 3 (2002): 209-272. https://doi.org/10.1016/S0376-0421(02)00005-2
[37] Oberkampf, William L., and Matthew F. Barone. "Measures of agreement between computation and experiment: validation metrics." *Journal of Computational Physics* 217, no. 1 (2006): 5-36. https://doi.org/10.1016/j.jcp.2006.03.037
[38] Tamura, Tetsuro, and Y. Itoh. "Unstable aerodynamic phenomena of a rectangular cylinder with critical section." *Journal of Wind Engineering and industrial Aerodynamics* 83, no. 1-3 (1999): 121-133. https://doi.org/10.1016/S0167-6105(99)00066-5
[39] Haque, Md Naimul, Hiroshi Katsuchi, Hitoshi Yamada, and Mayuko Nishio. "Numerical simulation for effects of wind turbulence on flow field around rectangular cylinder." *Journal of Structural Engineering A* 59 (2013): 605-615. https://doi.org/10.11532/structcivil.59A.605
[40] Knisely, Charles W. "Strouhal numbers of rectangular cylinders at incidence: a review and new data." *Journal of Fluids and Structures* 4, no. 4 (1990): 371-393. https://doi.org/10.1016/0889-9746(90)90137-T
[41] Hiroaki, Nishimura. "A study of the wind force on several rectangular prisms." *Journal of Applied Mechanics* 5 (2002): 689-698. https://doi.org/10.2208/journalam.5.689

[42] Nakamura, Yasuharu, and Katsuya Hirata. "Critical geometry of oscillating bluff bodies." *Journal of Fluid Mechanics* 208 (1989): 375-393. https://doi.org/10.1017/S0022112089002879

[43] Sumner, D., N. Rostamy, D. J. Bergstrom, and J. D. Bugg. "Influence of aspect ratio on the mean flow field of a surface-mounted finite-height square prism." *International Journal of Heat and Fluid Flow* 65 (2017): 1-20. https://doi.org/10.1016/j.ijheatfluidflow.2017.02.004

[44] Rastan, M. R., H. Shahbazi, A. Sohankar, Md Mahbub Alam, and Yu Zhou. "The wake of a wall-mounted rectangular cylinder: Cross-sectional aspect ratio effect." *Journal of Wind Engineering and Industrial Aerodynamics* 213 (2021): 104615. https://doi.org/10.1016/j.jweia.2021.104615

[45] Kawamura, Takao, Munehiko Hiwada, Toshiharu Hibino, Ikuo Mabuchi, and Masaya Kumada. "Flow around a finite circular cylinder on a flat plate: Cylinder height greater than turbulent boundary layer thickness." *Bulletin of JSME* 27, no. 232 (1984): 2142-2151. https://doi.org/10.1299/jsme1958.27.2142

[46] Tamura, T., and P. P. N. L. Dias. "Unstable aerodynamic phenomena around the resonant velocity of a rectangular cylinder with small side ratio." *Journal of Wind Engineering and Industrial Aerodynamics* 91, no. 1-2 (2003): 127-138. https://doi.org/10.1016/S0167-6105(02)00340-9

[47] McClean, J. F., and D. Sumner. "An experimental investigation of aspect ratio and incidence angle effects for the flow around surface-mounted finite-height square prisms." *Journal of Fluids Engineering* 136, no. 8 (2014). https://doi.org/10.1115/1.4027138

[48] Barata, La Ode Ahmad, Takahiro Kiwata, Takaaki Kono, and Toshiyuki Ueno. "Effects of span length and additional structure on flow-induced transverse vibration characteristic of a cantilevered rectangular prism." *Journal of Flow Control, Measurement & Visualization* 8, no. 3 (2020): 102-120. https://doi.org/10.4236/jfcmv.2020.83006

[49] Mizukami, Shunichi, Takahiro Kiwata, Takaaki Kono, Barata La Ode, and Toshiyuki Ueno. "Transverse Vibration Characteristics of a Rectangular Prism with Small Side Ratio and Flow Field around the Prism: Effect of Having or not Having an End of the Prism." *The Proceedings of Mechanical Engineering Congress, Japan* 2017 (2017). https://doi.org/10.1299/jsmemecj.2017.S0520506

[50] Ohya, Yuji. "Note on a discontinuous change in wake pattern for a rectangular cylinder." *Journal of Fluids and Structures* 8, no. 3 (1994): 325-330. https://doi.org/10.1006/jfls.1994.1015

[51] Barata, La Ode Ahmad, Kiwata Takahiro, Toshiyuki Ueno, Samhuddin Samhuddin, and La Hasanudin. "Experimental Investigation of Bladeless Power Generator from Wind-induced Vibration." *International Journal of Renewable Energy Development* 11, no. 3 (2022): 661-675.